Lamellar eutectic growth under forced convection: A phase-field lattice-Boltzmann study based on a modified Jackson-Hunt theory

Ang Zhang,[1] Jinglian Du,[1] Zhipeng Guo,[1,*] and Shoumei Xiong[1,2,†]

[1]*School of Materials Science and Engineering, Tsinghua University, Beijing 100084, People's Republic of China*

[2]*Key Laboratory for Advanced Materials Processing Technology, Ministry of Education, Tsinghua University, Beijing 100084, People's Republic of China*

(Received 15 March 2018; revised manuscript received 23 July 2018; published 2 October 2018)

Effect of forced convection on the lamellar eutectic growth was investigated by combining a modified Jackson-Hunt theory and a phase-field lattice-Boltzmann approach. Under the consideration of the asymmetrical tilting pattern and curvature effect, the classical eutectic Jackson-Hunt theory [Jackson and Hunt, Trans. Metall. Soc. AIME **236**, 1129 (1966)] was modified to better understand the physical mechanism driving the eutectic growth with convection. Results showed that the eutectic growth velocity increased linearly with increasing undercooling and exhibited a parabola trend versus the inverse of initial lamellar spacing. The flow induced by a horizontal external force tilted the eutectic lamellae by altering the solute distribution near the interface. Under weak convection, the phase-field lattice-Boltzmann simulation results agreed well with those predicted by the modified Jackson-Hunt theory. But under strong convection, the consistency of the two results was largely dependent on the alloy parameters and convection intensity.

DOI: 10.1103/PhysRevE.98.043301

I. INTRODUCTION

Investigation of eutectic growth against convection has been a popular but challenging subject for decades since the pioneering work by Jackson and Hunt (JH) [1–3]. The interaction of convection and growth kinetics of eutectic lamellae determines the local solute and/or thermal distribution, which significantly influences the ultimate properties of materials [4–6].

Extensive theoretical and experimental studies have been conducted to investigate the eutectic growth against melt convection. Quenisset *et al.* [7] proposed a simple model to predict the influence of forced convection on eutectic growth by assuming a laminar stationary flow parallel to the growth interface. Ma *et al.* [8] adopted the asymptotic expansion to solve the convection-diffusion eutectic equations under a low *Péclet* number. Lee *et al.* [3] performed experiments to investigate the spatiotemporal Al-Cu microstructure evolution under fluid flow. Nevertheless, the effect of fluid flow on eutectic growth still remains unclear. For example, most existing theoretical studies assumed that the eutectic growth direction would not be affected by the fluid flow [2,7,8], i.e., ignoring the lamellar tilt under convection. Numerical modeling on eutectic growth with convection has also long been contentious. Wang *et al.* [9] and Siquieri *et al.* [10] found that the eutectic growth direction would tilt towards the downstream side of the fluid flow by Monte Carlo and phase-field investigations, respectively. But Chen *et al.* [11] predicted that the eutectic lamellae would tilt towards the upstream side. Accordingly, a more sophisticated study is required to establish how the fluid flow interacts with the eutectic microstructure.

As a powerful numerical approach for simulating mesoscale microstructure, the phase-field model (PFM) has been successfully applied to simulate the eutectic phase transition [12–16]. By introducing so-called order parameters (i.e., the phase-field variables) to denote different phases, the evolution of the system can be described by a set of partial differential equations [17–19]. In comparison with other numerical models such as the cellular automaton, the interfacial Gibbs-Thomson effect can be recovered with high accuracy, and the explicit tracking of the phase interface is avoided [20], which makes the computations involving the interface evolution much easier to perform than sharp-interface models.

When incorporating the fluid flow in the PFM, a conventional method is to solve the Navier-Stokes (NS) equations. But the solving process is computationally expensive and easily becomes diverged when handling cases with high solid fraction (e.g., $>30\%$) [21,22]. To solve the coupled phase-field NS equations, Beckermann *et al.* [23] adopted a so-called SIMPLER algorithm, Tong *et al.* [24] used a multigrid SIMPLE method, Lan *et al.* [25] employed an adaptive finite volume method, and the current authors [26] previously used a parallel-multigrid approach. The principal difficulty for these attempts stems from the fact that the Poisson term in the NS equations needs to be implicitly and iteratively solved during each advancing step, which remarkably lowers the computing efficiency [22].

As an alternative, the lattice-Boltzmann model (LBM) is rooted in the mesoscopic kinetic theory [27], and has favorable advantages over the continuum NS solvers in phase-change problems, because the phase interfaces are inherently mesoscopic in nature [28]. In the LBM, a population

*Corresponding author: zhipeng_guo@mail.tsinghua.edu.cn

†smxiong@tsinghua.edu.cn

of pseudoparticles represented by a distribution function is introduced to describe the macroscopic transport [29–32]. With its attractive advantages including essentially parallelizable computing property, easy boundary setting, and higher stability, the LBM has been combined with dendritic PFM to simulate the dendritic growth with convection [33–36], and is first combined with the multiPFM to investigate the effect of natural convection on eutectic growth by the current authors [37].

From the computational viewpoint, however, the numerical solution on the phase transition involving interface evolution is a challenging subject. To resolve the solid-liquid (S-L) interface during solidification, the discretized mesh size must be as small as a nanometer, which induces gigantic computing overhead [38]. The solving process of the coupled phase-field equations also requires a high-fidelity numerical scheme. To this end, different methods have been developed to improve the computing efficiency, such as employing simplified models or material parameters [39,40], focusing on the interface by setting a cutoff in the bulk phases [41,42] or adopting a moving window technique [43,44]. However, using a uniform grid to discretize the governing equations in the whole computational domain is still inefficient and unnecessary [28]. Accordingly, a so-called adaptive mesh refinement (AMR) is developed. During simulation, the phase interface is the position where the high resolution is required, and thus the grids need to be refined, while the bulk phases can be demonstrated by the coarser grids. Based on the block-structured AMR mesh architecture, the current authors [22] developed a high performance computing scheme (named para-AMR in abbreviation) to solve the phase-field lattice-Boltzmann (PFLB) equations. The kernel of the scheme comprises a massive-parallel computing scheme and multilevel dynamic grid partitioning. Numerical tests confirm that this approach can improve the computing efficiency by two to three orders of magnitude without compromising any accuracy [22].

In this work, we couple the eutectic PFLB equations and the state-of-the-art para-AMR algorithm to investigate the effect of forced convection on eutectic growth. Under the consideration that the eutectic lamellar growth direction will be adjusted under convection, we revisit the JH theory by considering the lamellar asymmetrical tilting pattern. The curvature effect on the undercooling, which was simplified in most existing work [2,7,8], is also emphasized and reevaluated. Through detailed comparisons between the PFLB simulation results and the theoretical predictions, the effect of forced convection is explored, and several key mechanisms of eutectic growth under forced convection are highlighted.

The work is organized as follows. In Sec. II, the numerical method is briefly introduced, including the PFM, the LBM, and the AMR algorithm. In Sec. III, a modified JH theory is derived by considering the asymmetrical tilting pattern and interfacial curvature effect. In Sec. IV, the PFLB simulation results are presented and discussed. The comparisons between the PFLB simulation results and the theoretical predictions using the modified JH theory are presented in Sec. V. Concluding remarks are provided in Sec. VI.

II. METHODOLOGY

The simulation configuration in this work is similar to our recent work [37], and only main features are provided as follows. Further details including the modeling equations and discretization methods in the PFM, the discrete velocity model in the LBM, the validation of the PFLB model, and the detailed para-AMR algorithm structure can be found in [15,22,37,38].

A. Phase-field model

The eutectic phase-field model proposed by Kim *et al.* [13] is extended to simulate two-phase growth in the presence of convection. The eutectic model was developed based on an interface-field concept [45] and equal chemical potential among the coexisting phases. Three phase-field variables ϕ_i $(i = 1, 2, 3)$ with a sum of 1 are introduced to denote different phases, e.g., $\phi_3 = 1$ and $\phi_1 = \phi_2 = 0$ denote the liquid phase. To incorporate the convective flux in the model, the diffusion equation is modified by considering the melt convection [24,26], i.e.,

$$\partial_t C + \phi_3 \vec{v} \cdot \nabla C = \nabla \cdot \left(D \sum_i \phi_i \nabla C_i \right), \tag{1}$$

where $C(x,t) = \sum_i \phi_i \nabla C_i$ is the average concentration of coexisting phases and determined by a weighted average. The phase-field variable ϕ_3 represents the liquid fraction, $\vec{v}$ is the intrinsic flow velocity induced by an external force, which is expanded as $\vec{v} = (u, v)$ in the two-dimensional (2D) case and calculated using the LBM. $D = \phi_3 D_l + (1 - \phi_3) D_s$ is the diffusivity dependent on the phase field, where D_l and D_s are the solute diffusivity in the liquid and solid phases, respectively.

It is noted that the phase field is not convective [10,24] and thus the governing equation remains unchanged. The temperature is set to be isothermal, i.e., ignoring the thermal diffusion because the thermal diffusivity is normally four orders of magnitude larger than the solute diffusivity [37].

B. Lattice-Boltzmann model

As a mesoscopic kinetic-based scheme, the LBM describes the flow evolution through a relaxation of momentum to a local equilibrium, and characterizes the macroscopic transport process by repeated streaming and collision of a series of pseudoparticles [29].

A widely used two-dimensional nine-velocity (named D2Q9) model [46] is employed to determine the incompressible fluid flow,

$$f_i(\vec{r} + \vec{c}_i \delta t, t + \delta t) = f_i(\vec{r}, t) - \left[f_i(\vec{r}, t) - f_i^{\mathrm{eq}}(\vec{r}, t) \right] / \tau + G_i(\vec{r}, t) \delta t \tag{2a}$$

$$\text{with } f_i^{\mathrm{eq}} = \rho w_i \left(1 + \frac{3\vec{c}_i \cdot \vec{v}}{c^2} + \frac{9(\vec{c}_i \cdot \vec{v})^2}{2c^4} - \frac{3\vec{v} \cdot \vec{v}}{2c^2} \right), \tag{2b}$$

where $\vec{c}_i$ is the discrete velocity along the ith direction, δt is the time step, τ is the relaxation time during the collision process, c is the lattice speed, and w_i is the weight coefficient

to guarantee the mass and momentum conservation. $f_i(\vec{r},t)$ is the particle distribution function along the ith direction at the position $\vec{r}$ and time t, and $f_i^{\rm eq}(\vec{r},t)$ is the corresponding equilibrium distribution function. The discrete force $G_i(\vec{r},t)$ with second-order accuracy can be given by [37,47]

$$G_i = \left(1-\frac{1}{2\tau}\right)w_i\left(\frac{3(\vec{c}_i-\vec{v})}{c^2}+\frac{9(\vec{c}_i\cdot\vec{v})\vec{c}_i}{c^4}\right)\cdot(G_D+G_F), \tag{3a}$$

$$G_D(\vec{r},t) = -2\rho\upsilon h\phi_3(1-\phi_3)^2\vec{v}/W_0^2, \tag{3b}$$

$$G_F(\vec{r},t) = A\rho\phi_3\vec{e}, \tag{3c}$$

where $\rho=\sum_i f_i$, $\vec{v}=\sum_i f_i\vec{c}_i/\rho+(G_D+G_F)\delta t/(2\rho)$ is the flow velocity, and G_D is the dissipative drag force to satisfy the no-slip boundary condition near the S-L interface, which behaves as a distributed momentum sink that vanishes the velocity as the liquid fraction (i.e., ϕ_3) approaches 0 [24]. $h=2.757$ is a dimensionless constant [23], W_0 is the interface thickness, and $\upsilon=c^2\delta t(2\tau-1)/6$ is the kinematic viscosity. G_F is the horizontal external force controlling the fluid flow, A is the amplitude of the external force, and $\vec{e}$ is the unit vector along the x^+. It is noted that the flow in this work is induced by imposing an external force inside the melt, i.e., like that in practical scenarios such as electromagnetic or mechanical stirring.

C. Numerical algorithm

The para-AMR algorithm comprises three ingredients, i.e., hierarchical mesh architecture with adaptivity, data communication between different patchboxes and grid levels, and the parallel partitioning of the computing data. Detail of the para-AMR algorithm has been presented in our earlier work [15,16,19,22,36–38,48–51], and in this study, only a brief introduction is given here.

The essence of the AMR is tagging the potential grids according to a gradient criterion [38],

$$\max_{1\leqslant i\leqslant 3}(|\nabla\phi_i|)+E_c|\nabla C|+E_v\left(\sqrt{|\nabla u|^2+|\nabla v|^2}\right)\geqslant\xi, \tag{4}$$

where E_c and E_v are the weight coefficients for the solute and velocity respectively, ξ is a threshold value determined via numerical tests, and u and v are the two axial velocity components. A cluster algorithm developed by Berger and Rigoutsos [52] is adopted to separate the tagged points into patchboxes. After constructing a hierarchical architecture with different sets of patchboxes on each grid level, the local data are broadcast to all processors to realize the parallel computation.

In the AMR, grids with higher resolution are preferred where a more accurate solution is anticipated. During the eutectic growth, the phase interface is the position where the grids need to be refined, and a much coarser grid can be used away from the interface. Figure 1 shows a typical three-level hierarchical data structure superimposed on the cloud picture of the solute field, in which the arrows denote the velocity vector of the flow field. The layout of the patchboxes is depicted using the thicker solid lines, in which the meshes with same size are filled. The adjustment of the patchbox density and mesh distribution clearly illustrates that the mesh

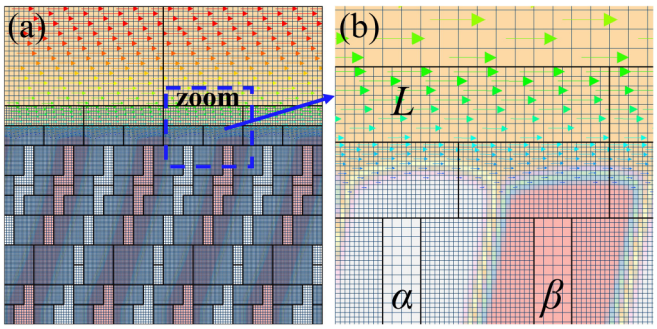

FIG. 1. Typical three-level hierarchical data structure superimposed on the cloud picture of the solute field.

refinement can perfectly characterize the phase interface, as shown in the local enlarged image in Fig. 1(b). It is noted that because of the introduced diffuse interface in the PFM, a remarkable transition layer exhibits between the bulk phases, i.e., at the α-L, β-L, and α-β interfaces.

After each iteration, the calculated velocity using the LBM must be scaled back by multiplying $dx_{\rm max}/dt$ to match the unit of the phase-field variables, where $dx_{\rm max}$ and dt are the maximum grid size in the multilevel architecture and the time step during simulation, respectively [22].

III. MODIFIED JACKSON-HUNT THEORY

Since the classical steady-state eutectic growth theory was established by Jackson and Hunt [1], several authors have proposed different modifications to incorporate the effect of fluid flow [2,7,8,53]. In those theoretical analyses, assumptions were made to simplify the model, which however ignored certain important physics during solidification. For example, Quenisset *et al.* [7] and Baskaran *et al.* [2] assumed that the curvature undercooling was inversely proportional to the lamellar spacing, i.e., ignoring the adjustment of the interfacial curvature. Ma *et al.* [8] discussed the effect of convection without considering the change of lamellar growth direction, which was inappropriate because eutectic lamellae can adjust or tilt their directions under forced convection.

Similar to Ma *et al.* [8], in this work, an asymptotic expansion method is used to obtain the approximate solution of the convection-diffusion equation governing the eutectic growth. The S-L interface is assumed to be planar and the flow parallel to the lamellae is ignored [2,8]. The steady-state solute field $C(x,y)$ near the interface satisfies [7]

$$D_l\nabla^2 C+V\frac{\partial C}{\partial y}-u\frac{\partial C}{\partial x}=0, \tag{5a}$$

where V is the longitudinal growth velocity, and u is the transverse flow velocity at a distance y away from the interface and expressed as $u=yG_u=y\partial u/\partial y$, where G_u is the velocity gradient and is assumed constant as suggested by Baskaran *et al.* [2] and Caram *et al.* [54]. The coordinate system (x,y) is defined as follows: y denotes the distance away from the S-L interface, and x starts from the midpoint of the α-L interface (see Fig. 2). Accordingly, the α phase ranges from $-S_{\alpha L}$ to $S_{\alpha L}$ while the β phase ranges from $S_{\alpha L}$ to $S_{\alpha L}+2S_{\beta L}$, where

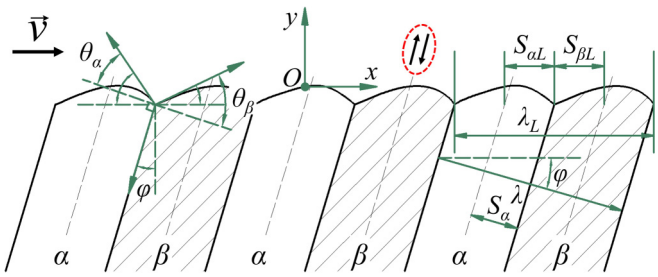

FIG. 2. Schematic diagram of lamellar eutectic growth under forced convection.

$S_{\alpha L}$ and $S_{\beta L}$ are the interfacial half width of the α and β phases respectively.

To reduce the number of unknowns in Eq. (5a), a nondimensional treatment is taken by defining the dimensionless length $X = x/\lambda_L$ and $Y = y/\lambda_L$ [2],

$$\frac{\partial^2 C}{\partial X^2} + \frac{\partial^2 C}{\partial Y^2} + \Lambda \frac{\partial C}{\partial Y} - Y\Theta \frac{\partial C}{\partial X} = 0, \tag{5b}$$

where λ_L is the interfacial lamellar width (not the lamellar spacing λ), $\Lambda = \lambda_L V/D_l$ is the dimensionless interfacial lamellar width, and $\Theta = G_u \lambda_L^2/D_l$ is the dimensionless flow velocity and it measures the convection intensity.

It is noted that Eq. (5b) is a nonhomogeneous partial differential equation, the solution of which can be designated by summing its special solution $C^*(X, Y)$ and the general solution $C_0(X, Y)$ of the associated homogeneous equation [i.e., omitting the convection term $Y\Theta \cdot \partial C/\partial X$ in Eq. (5b)],

$$C(X, Y) = C^*(X, Y) + C_0(X, Y), \tag{6}$$

where $C_0(X, Y)$ is actually the solution of the classical JH theory [1], i.e.,

$$C_0(X, Y) = C'_\infty + \sum_{n=0}^{\infty} B'_n \cos(2n\pi X) \times \exp\left(-\frac{\Lambda Y}{2} - \sqrt{\left(\frac{\Lambda Y}{2}\right)^2 + (2n\pi Y)^2}\right), \tag{7a}$$

which is reduced to the following equation in terms of $\Lambda \ll 4n\pi$ during the practical solidification process,

$$C_0(X, Y) = C'_\infty + B'_0 \exp(-\Lambda Y) + \sum_{n=1}^{\infty} B'_n \cos(2n\pi X) \exp(-2n\pi Y), \tag{7b}$$

where C'_∞, B'_0, and B'_n depend on the boundary conditions. C'_∞ will be determined later, and B'_0 and B'_n are determined by using the orthogonality of trigonometric functions (detailed in Appendix A), i.e.,

$$B'_0 = \frac{S_{\alpha L} C_L^\alpha (1 - k_\alpha) + S_{\beta L} C_L^\beta (1 - k_\beta)}{(1 + \Theta)(S_{\alpha L} + S_{\beta L}) \cos\varphi}, \tag{7c}$$

$$B'_n = \frac{\Lambda\left[C_L^\alpha (1 - k_\alpha) - C_L^\beta (1 - k_\beta)\right]}{(1 + \Theta)(n\pi)^2 \cos\varphi} \sin\left(\frac{n\pi S_{\alpha L}}{S_{\alpha L} + S_{\beta L}}\right), \tag{7d}$$

where $k_\alpha < 1$ and $k_\beta > 1$ are the equilibrium partition coefficients of the α and β phases, respectively. C_L^α and C_L^β are the liquid concentration in equilibrium with the α and β phases at a given temperature respectively, both of which can be assumed to be the eutectic concentration C_E for a lower undercooling.

If the convection intensity Θ is small, an approximation solution of $C^*(X, Y)$ is presented by an asymptotic expansion method based on the power series [55]

$$C^*(X, Y) = \sum_{k=1}^{\infty} \Theta^k C_k(X, Y). \tag{8}$$

Inserting Eq. (8) into Eq. (6) and then replacing $C(X, Y)$ in Eq. (5b) with the new Eq. (6) yield

$$\frac{\partial^2 C_0(X, Y)}{\partial X^2} + \frac{\partial^2 C_0(X, Y)}{\partial Y^2} + \Lambda \frac{\partial C_0(X, Y)}{\partial Y} + \sum_{k=1}^{\infty} \Theta^k \left(-Y \frac{\partial C_{k-1}(X, Y)}{\partial X} + \frac{\partial^2 C_k(X, Y)}{\partial X^2} + \frac{\partial^2 C_k(X, Y)}{\partial Y^2} + \Lambda \frac{\partial C_k(X, Y)}{\partial Y}\right) = 0. \tag{9a}$$

Typically, the larger the index k of Θ, the more precise the solution. However, since Θ is small, the first order is sufficient to obtain an exact solute field [8]. Considering $C_0(X, Y)$ is the general solution, Eq. (9a) is reduced to

$$\frac{\partial^2 C_1(X, Y)}{\partial X^2} + \frac{\partial^2 C_1(X, Y)}{\partial Y^2} + \Lambda \frac{\partial C_1(X, Y)}{\partial Y} - Y \frac{\partial C_0(X, Y)}{\partial X} = 0 \tag{9b}$$

Inserting Eq. (7b) into Eq. (9b) and solving the nonhomogeneous equation in the same way as discussed before, the special solution becomes (detailed in the Appendix B)

$$C_1(X, Y) = C_0(X, Y) + \left(\frac{Y}{\Lambda} - \frac{2}{\Lambda^2}\right) \sum_{n=1}^{\infty} B'_n \sin(2n\pi X) \times \exp(-2n\pi Y). \tag{10}$$

Accordingly, we obtain the asymptotic expansion solution of Eq. (5b) by combining Eqs. (6), (7b), (8), and (10),

$$C(X, Y) = (1 + \Theta) C'_\infty + (1 + \Theta) B'_0 \exp(-\Lambda Y) + (1 + \Theta) \sum_{n=1}^{\infty} B'_n \left[\cos(2n\pi X) + \frac{\Theta}{1 + \Theta}\left(\frac{Y}{\Lambda} - \frac{2}{\Lambda^2}\right) \sin(2n\pi X)\right] \exp(-2n\pi Y). \tag{11}$$

As discussed, when the forced convection is considered into the eutectic growth, the lamellae change from the symmetrical pattern to the asymmetrical tilting state with respect to the centerlines of the solid phases. Now that the lamellar tilting angle φ is not equal to 0, the precipitating process of the eutectic components will proceed along the direction of the tilting angle (see the dashed red circles in Fig. 2), and the transfer of the precipitated elements will comprise two parts, i.e., some diffusing to the interior of the liquid phase and the others convected away by flow. Accordingly, the flux balance of the steady-state eutectic growth is modified; taking the α-L interface for instance, it should satisfy

$$-D_l \frac{\partial C}{\partial y}\bigg|_{y=0} + u\left(C_L^{\alpha} - C_{y=0}\right) = \frac{V}{\cos\varphi} C_L^{\alpha}(1-k_{\alpha}), \quad (12)$$

where $C_{y=0}$ is the interfacial solute concentration.

The boundary conditions and the flux conditions near the S-L interface satisfy

$$C|_{Y=\infty} = C_{\infty}, \quad (13a)$$

$$C|_{X=0} = C|_{X=1}, \quad (13b)$$

$$-\frac{S_{\alpha L}}{\lambda} < X < \frac{S_{\alpha L}}{\lambda}, \quad \frac{\partial C}{\partial Y}\bigg|_{Y=0} = -\frac{\Lambda C_L^{\alpha}(1-k_{\alpha})}{\cos\varphi}, \quad (13c)$$

$$\frac{S_{\alpha L}}{\lambda} < X < 1 - \frac{S_{\alpha L}}{\lambda}, \quad \frac{\partial C}{\partial Y}\bigg|_{Y=0} = -\frac{\Lambda C_L^{\beta}(1-k_{\beta})}{\cos\varphi}, \quad (13d)$$

where C_{∞} is the dimensionless concentration far from the interface, namely the initial concentration. Eq. (13b) denotes the periodic boundary condition, i.e., the solute field repeats for each lamellar width. $-S_{\alpha L}/\lambda < X < S_{\alpha L}/\lambda$ is over the α phase while $S_{\alpha L}/\lambda < X < 1 - S_{\alpha L}/\lambda$ is over the β phase. It is noted that the second term on the left of Eq. (12) is removed because the velocity at the S-L interface is zero.

Based on the far-field boundary condition Eq. (13a), we determine $C(X,\infty) = (1+\Theta)C'_{\infty} = C_{\infty}$. Inserting Eqs. (7c) and (7d) into Eq. (11) and assuming $C_L^{\alpha} = C_L^{\beta} = C_E$ for a lower undercooling, we obtain the asymptotic expansion solution of Eq. (5b),

$$C(X,Y) = C_{\infty} + \frac{B_0}{\cos\varphi}\exp(-\Lambda Y) + \sum_{n=1}^{\infty}\frac{B_n}{\cos\varphi}\Bigg[\cos(2n\pi X) + \frac{\Theta}{1+\Theta}\left(\frac{Y}{\Lambda} - \frac{2}{\Lambda^2}\right)\sin(2n\pi X)\Bigg]\exp(-2n\pi Y), \quad (14)$$

where

$$B_0 = C_E - \frac{S_{\alpha L}k_{\alpha} + S_{\beta L}k_{\beta}}{S_{\alpha L} + S_{\beta L}}C_E, \quad (15a)$$

$$B_n = \frac{\Lambda C_E(k_{\beta} - k_{\alpha})}{(n\pi)^2}\sin\left(\frac{n\pi S_{\alpha L}}{S_{\alpha L} + S_{\beta L}}\right). \quad (15b)$$

From Eq. (14), the solute concentration near the S-L interface is obtained,

$$C(X,0) = C_{\infty} + \frac{B_0}{\cos\varphi} + \sum_{n=1}^{\infty}\frac{B_n}{\cos\varphi} \times \left(\cos(2n\pi X) - \frac{2\Theta}{\Lambda^2(1+\Theta)}\sin(2n\pi X)\right). \quad (16)$$

The average interfacial solute concentration of the α and β phases can be deduced as follows:

$$\overline{C_{\alpha}} = \frac{\lambda_L}{2S_{\alpha L}}\int_{-S_{\alpha L}/\lambda}^{S_{\alpha L}/\lambda} C(X,0)dX = C_{\infty} + \frac{B_0}{\cos\varphi} + \frac{\lambda_L \Lambda C_E(k_{\beta} - k_{\alpha})}{2S_{\alpha L}\cos\varphi}P, \quad (17a)$$

$$\overline{C_{\beta}} = \frac{\lambda_L}{2S_{\beta L}}\int_{S_{\alpha L}/\lambda}^{1-S_{\alpha L}/\lambda} C(X,0)dX = C_{\infty} + \frac{B_0}{\cos\varphi} - \frac{\lambda_L \Lambda C_E(k_{\beta} - k_{\alpha})}{2S_{\beta L}\cos\varphi}P, \quad (17b)$$

where

$$P = \sum_{n=1}^{\infty}\frac{1}{(n\pi)^3}\sin^2\left(\frac{n\pi S_{\alpha L}}{S_{\alpha L} + S_{\beta L}}\right). \quad (17c)$$

It is noted that the presence of forced convection makes the interface shape become asymmetrical about the centerline of solid phases. Thus, when determining the average solute concentration, the integrating range is a complete width of solid phase (e.g., from $-S_{\alpha L}$ to $S_{\alpha L}$ for the α phase), rather than only half in [8] (e.g., from 0 to $S_{\alpha L}$ for the α phase).

In terms of the various factors contributing to the average undercooling, the interfacial undercooling ΔT at any point can be described as

$$\Delta T = T_E - T = \Delta T_c + \Delta T_r + \Delta T_k, \quad (18)$$

where T_E is the eutectic temperature and T is the interfacial actual temperature. $\Delta T_c = m[C_E - C(x)]$ is the constitutional undercooling, which denotes the deviation of the local composition from the eutectic composition, and m is the liquidus slope. $\Delta T_r = \Gamma\kappa(x)$ is the curvature undercooling reflecting the effect of the interfacial shape, where Γ is the Gibbs-Thompson coefficient, and $\kappa(x)$ is the local interfacial curvature. ΔT_k is the kinetic undercooling and can be reasonably ignored for most regular eutectic systems solidifying at low velocities when comparing with ΔT_c and ΔT_r [1,56].

Taking the α-L interface for instance, the interfacial average curvature can be described as

$$\langle\kappa_{\alpha}(x)\rangle = \frac{1}{2S_{\alpha L}}\int_{-S_{\alpha L}}^{S_{\alpha L}}\kappa_{\alpha}(x)dx = \frac{1}{2S_{\alpha L}}\int_{-S_{\alpha L}}^{S_{\alpha L}}\frac{|d^2I/dx^2|}{(1+(dI/dx)^2)^{3/2}}dx = \frac{\sin\theta_{\alpha}\cos\varphi}{S_{\alpha L}}, \quad (19)$$

where $\langle\cdot\rangle$ denotes the average operation, and the function $I(x)$ is used to describe the interfacial shape. θ_α is the contact angle between the α and liquid phase at the triple point. Detailed derivation of the average curvature is provided in Appendix C.

By inserting Eqs. (17a), (17b), and (19) into Eq. (18), the average undercooling near the S-L interface is determined as follows:

$$\Delta T_\alpha = m_\alpha\left[C_\infty - C_E + \frac{B_0}{\cos\varphi} + \frac{\lambda_L \Lambda C_E(k_\beta - k_\alpha)}{2S_{\alpha L}\cos\varphi}P\right] + \Gamma_\alpha\frac{\sin\theta_\alpha\cos\varphi}{S_{\alpha L}}, \tag{20a}$$

$$\Delta T_\beta = m_\beta\left[C_E - C_\infty - \frac{B_0}{\cos\varphi} + \frac{\lambda_L \Lambda C_E(k_\beta - k_\alpha)}{2S_{\beta L}\cos\varphi}P\right] + \Gamma_\beta\frac{\sin\theta_\beta\cos\varphi}{S_{\beta L}}, \tag{20b}$$

where m_α and m_β are the liquidus slopes of the α and β phases, and Γ_α and Γ_β are the Gibbs-Thompson coefficients of the α-L and β-L interfaces, respectively. θ_β is the contact angle between the β and liquid phases at the triple point. Since $\Delta T_\alpha = \Delta T_\beta$, Eqs. (20a) and (20b) can be simplified as

$$\frac{\Delta T}{m} = \frac{V\lambda_L Q}{\cos\varphi} + \frac{a\cos\varphi}{\lambda_L}, \tag{21}$$

where m, Q, a are constants given by

$$\frac{1}{m} = \frac{1}{m_\alpha} + \frac{1}{m_\beta}, \tag{22a}$$

$$Q = \frac{P(1+\zeta)^2 C_E(k_\beta - k_\alpha)}{\zeta D_l}, \tag{22b}$$

$$a = 2(1+\zeta)\left(\frac{\Gamma_\alpha\sin\theta_\alpha}{m_\alpha} + \frac{\Gamma_\beta\sin\theta_\beta}{\zeta m_\beta}\right), \tag{22c}$$

where $\zeta = S_{\beta L}/S_{\alpha L}$ is the ratio of the interfacial lamellar width. Clearly, Eqs. (22a)–(22c) are identical to those derived by Jackson and Hunt [1].

The classical JH theory is modified by replacing the lamellar spacing λ with the interfacial lamellar width λ_L and introducing lamellar tilting angle φ to characterize the effect of the single-direction forced convection. When $\varphi = 0$, we get $\lambda_L = \lambda$, and the modified JH theory is actually restored to the classical one.

IV. PHASE-FIELD LATTICE-BOLTZMANN SIMULATION RESULTS

Two typical eutectic alloys including the Al-Cu and CBr_4-C_2Cl_6 alloys were simulated, the thermophysical parameters of which can be found in our recent work [37]. The initial solute concentration C_0 was 0.173 mol frac for the Al-Cu alloy, and 0.118 mol frac for the CBr_4-C_2Cl_6 alloy, respectively. The undercooling was 1.0 and 0.05 K for the two alloys respectively unless stated otherwise. The minimum mesh size was 0.2 μm, and four eutectic couples were initialized at the bottom of the square computational domain filled with undercooled melt. For all variables including the phase field, solute, and velocity, a periodic boundary condition was set along the direction parallel to the S-L interface. Along the direction perpendicular to the S-L interface, a zero-Neumann boundary condition was set at both sides for the phase field and solute, while for the velocity, a no-slip condition was applied at the bottom and a specular reflection boundary condition was set at the top. In addition, a bounce-back scheme [57] is implemented at the moving S-L interface, i.e., $f_i(\vec{r}, t, \vec{c}_i) = f_i(\vec{r}, t, -\vec{c}_i)$.

A. Solute field and velocity field

Figure 3 shows typical simulation results including both the solute and velocity fields. The imposed external force was along the x^+ [see Eq. (3c)], which induced a left-to-right flow. Two solid phases (i.e., the α and β phases) simultaneously grew into the undercooled melt at a certain angle φ with the y^+. Figure 3(b) shows the distribution of the velocity isolines superimposed on the solute concentration isolines, in which the corresponding cloud picture of the flow field is inserted at the upper-right corner. The red arrows in Fig. 3(b) pointed to a direction with increasing velocity. Influenced by the interface

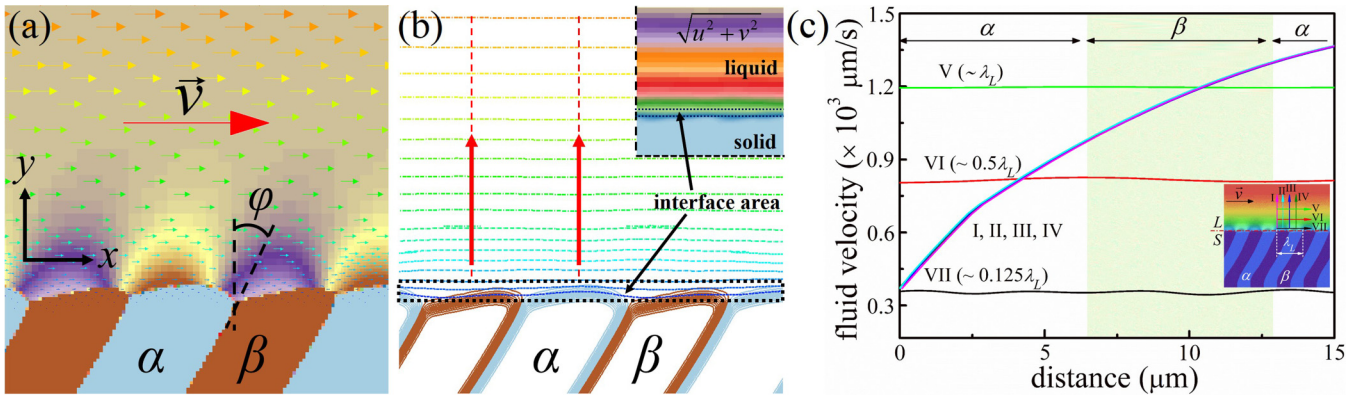

FIG. 3. (a) Simulated cloud picture of the solute field. The arrows denote the velocity vector. (b) Simulated velocity isolines superimposed on the solute concentration isolines. The cloud picture of the flow field is inserted at the upper-right corner. (c) Simulated fluid velocity versus the distances along different directions, i.e., the directions I–VII as designated by the arrows in the inserted cloud picture of the flow field superimposed on the solute field.

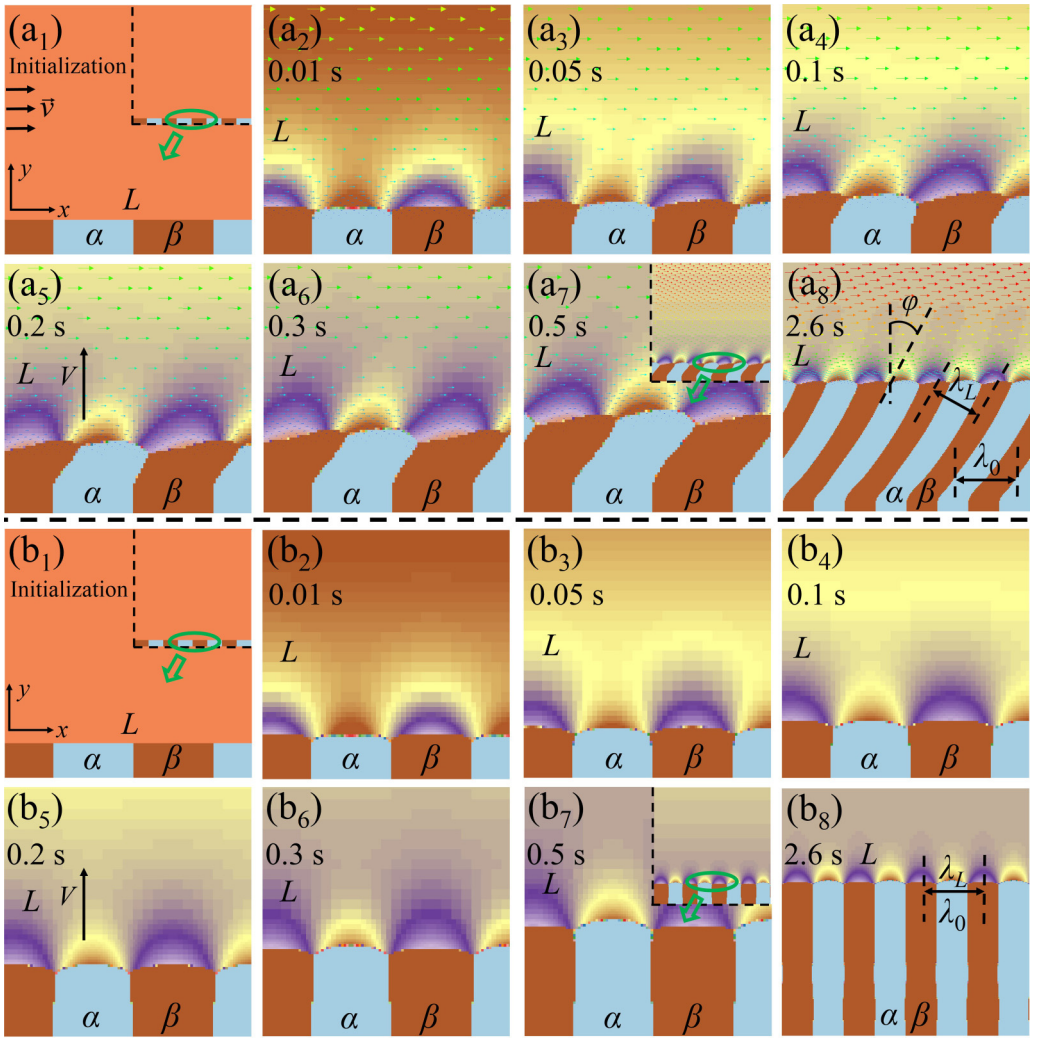

FIG. 4. Evolution of solute field under (a) forced convection and (b) nonconvection conditions.

shape and the dissipative drag force, the velocity isolines at the interfacial region were not strictly horizontal.

Figure 3(c) shows the fluid velocity versus the distance along different directions, i.e., the directions I–VII as designated by the arrows in the inserted cloud picture. In particular, the directions I–IV were perpendicular to the S-L interface and started at a certain distance, i.e., $0.125\lambda_L$, away from the top of the α-L interface, the triple point, the top of the β-L interface, and another adjacent triple point, respectively. The maximum velocity was 1.36×10^3 μm/s, and the four velocity-distance curves were overlapped, indicating that the velocity magnitude was only dependent on the vertical distance away from the S-L interface. The other three velocity-distance curves, as designated by V–VII, further validated this behavior. The locations of V–VII were parallel to the S-L interface with a distance of $0.125\,\lambda_L$, $0.5\,\lambda_L$, and λ_L away from the S-L interface, respectively. As the distance increased, the three velocity curves became flatter, and after approaching λ_L, the velocity barely changed (see the curve V). In this respect, the velocity changed slightly along the horizontal direction, or in other words, the fluid flow induced by the horizontal external force was close to a shear flow.

Figure 4 shows the evolution of the solute field under forced convection and nonconvection conditions from the initial state presented at the upper-right corner of Figs. 4(a_1) and 4(b_1), respectively. The lamellar couples circled by the solid olive line were locally enlarged, and Figs. 4(a_8) and 4(b_8) show the final entire morphologies. When the external force was along the x^+, i.e., from left to right, the eutectic lamellae tilted towards the x^+ in contrast with those under nonconvection condition, which agreed well with those simulated by Siquieri *et al.* [10] and Wang *et al.* [9]. The forced convection altered the interfacial morphology, and as time evolved, the lamellae became tilting and reached a steady state at 0.5 s, or after 200 000 steps in Fig. 4(a_7).

Figure 5(a) shows the distribution of the solute concentration near the interface, as designated by H_1 and H_2, for conditions without and with convection, respectively. The insets are the grayscale contour maps of the solute field, and the dark promotes the growth of the α phase. The presence of convection extended both maximum and minimum values of the solute concentration, which agreed with the additional sinusoidal terms in Eqs. (14) and (16). The solute concentration under convection became asymmetrical about the centerlines of the solid phases. In particular, the concentration close

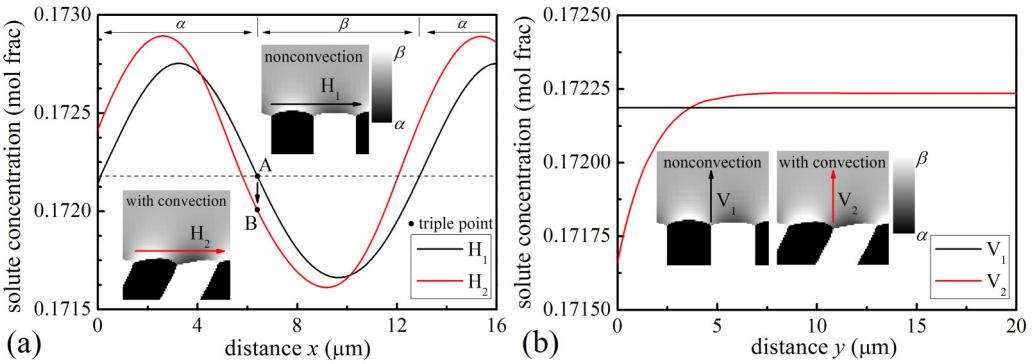

FIG. 5. Distribution of solute concentration along the given directions, i.e., H_1 and H_2 for the horizontal direction, and V_1 and V_2 for the longitudinal direction, respectively. The insets are the grayscale contour maps of the solute field with and without convection, in which the dark color favors the growth of the α phase.

to the right triple point of the α phase decreased from the equilibrium value (i.e., designated by A) to a lower value (i.e., designated by B). Accordingly, for the α phase, the solute concentration on the right of the centerline was lower than that on the left, promoting tilting eutectic growth mode. Figure 5(b) shows the solute concentration versus the distance along two vertical lines, as designated by V_1 and V_2, respectively. The solute concentration on the top of the triple point kept constant for the condition without convection. The presence of convection lowered the solute concentration near the right triple point of the α phase, i.e., accumulating more solvent elements which promoted the growth of the α phase. It is noted that the equilibrium solute concentration was lower than the initial eutectic concentration due to the solute redistribution near the interface (detailed in Appendix D).

B. Effect of computational domain

As shown in Fig. 3(c), the magnitude of the fluid velocity increased with the distance away from the *S*-*L* interface. According to the simulation configuration, the larger the vertical height of the computational domain, the greater the maximum velocity. Figures 6(a)–6(e) show the cloud pictures of the solute field in different computational domains, the sizes of which were varied as 51.2×51.2, 102.4×51.2, 51.2×102.4, 102.4×102.4, and $51.2 \times 153.6\,\mu m^2$, respectively. When the domain height was the same, e.g., Figs. 6(a) and 6(b) [or Figs. 6(c) and 6(d)], the eutectic lamellae presented similar growth patterns. However, when the height was increased, e.g., from Figs. 6(a) and 6(c) to 6(e), the lamellar tilting angle increased from 28° and 45° to 52° under the same external force, i.e., the same amplitude A in Eq. 3(c).

Figure 6(f) shows the velocity magnitude versus the distance away from the *S*-*L* interface. The velocity increased from 0 at the *S*-*L* interface to the maximum at the top side. For the domain with larger height [e.g., case III in Fig. 6(f)], the flow velocity had larger value and exhibited wider variation range. Accordingly, the eutectic lamellae tilted more significantly towards the flow direction. To avoid such effect, the subsequent phase-field simulations were all performed in domains with the same height.

C. Eutectic tilting growth

During lamellar eutectic growth, the coexisting solid phases grow into the undercooled melt simultaneously,

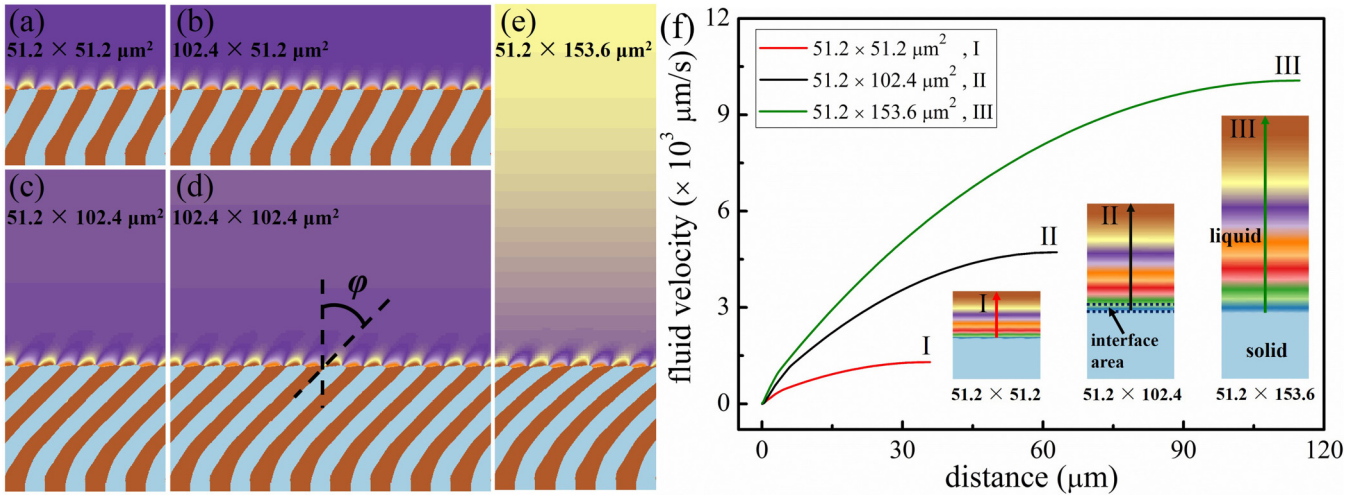

FIG. 6. (a)–(e) Simulated solute field with different computational domain sizes. (f) Simulated fluid velocity vs the distance away from the *S*-*L* interface. The insets are the corresponding flow fields.

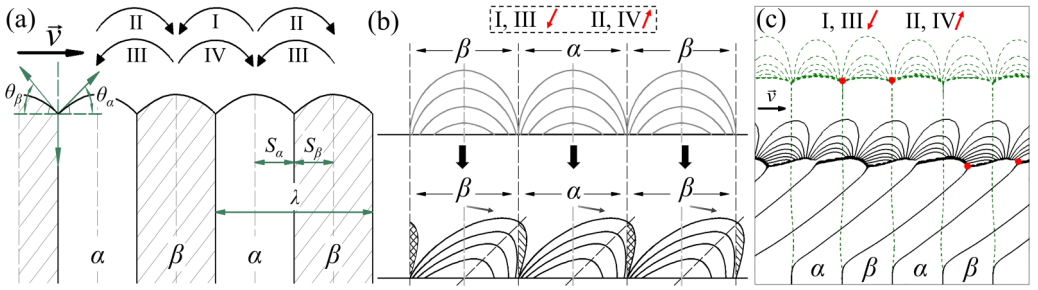

FIG. 7. (a),(b) Schematic diagrams of the eutectic growth and lamellar tilt. (c) Illustration for the effect of the forced convection on concentration isolines.

forming a stable solute transition layer. Because of the difference of the solute concentration in the layer, a lateral solute transfer exhibits between lamellae (i.e., the solute transport couple I and II or the couple III and IV), which maintains the cooperative growth of the coexisting solid phases, as shown in Fig. 7(a).

Under a periodic boundary condition for all variables including the phase field, solute, and velocity, the presence of a left-to-right forced convection enhanced the solute transport couple II and IV, but weakened I and III instead. In other words, the solute transport couple moved towards the downstream side, which made the lamellae tilt towards the downstream side as well, as shown in Fig. 7(b). Figure 7(c) shows an illustration diagram for the effect of the forced convection on the concentration isolines. Comparing with the case without flow [see the dashed lines in Fig. 7(c)], the solute isolines shifted along the flow direction [see the solid lines in Fig. 7(c)], indicating that the direction along which the concentration varied the slowest changed. Furthermore, with convection, the solute concentration at the triple point no longer equaled the equilibrium concentration, as designated by the solid red circles in Fig. 7(c).

To further investigate the effect of forced convection, the amplitude A in Eq. (3c) was changed to induce flow with different intensities. A/A_0 was employed to denote the intensity of the flow, where A_0, determined *via* numerical tests, corresponded to the external force which only tilted the lamellae 0.5°, i.e., had a negligible effect on the eutectic growth. Figure 8(a) shows the interface morphologies under different flow intensities. Those morphological curves were extracted according to $\phi_3 = 0.5$ and $t = 2.6$ s (i.e., 1 000 000 time steps). The larger the flow intensity, the more significant the asymmetry of the interface morphology. In particular, as the flow intensity increased, the distance between the highest point of the shape curve and the triple point became increasingly small [see the distances d_0–d_5 in Fig. 8(a)], indicating that the offset of the concentration isolines increased with convection intensity. The asymmetrical interface shape demonstrated the existence of a transverse drift of eutectic lamellae, which could be characterized by a drift velocity V_d, i.e., $V_d = V \tan\varphi$. Figure 8(b) shows the growth velocity including V and V_d and the maximum flow velocity $|\vec{v}|_{\max}$ versus the convection intensity. As the flow intensity increased, the longitudinal growth velocity V decreased, but both the maximum flow velocity and the drift velocity V_d increased, indicating the lamellar tilting angle was enlarged. When the intensity was magnified by 4000 times, V_d exceeded V, indicating that the lamellar tilting angle was larger than 45°.

It is noted that the flow direction is dependent on the boundary condition. Figure 9 shows the evolution of the eutectic lamellae under a zero-Neumann boundary condition for the solute and phase fields, and a no-slip boundary condition for the flow field. The initial state was the same as that in Fig. 4, as shown at the upper-right corner of Fig. 9(a). Different from the transverse flow under the periodic side boundary condition, the convection induced by the external force formed a semicircular vortices in the remaining liquid region. The moving direction of the solute transport couple exhibited no regularity [i.e., not single-direction move in Fig. 4(a)], and

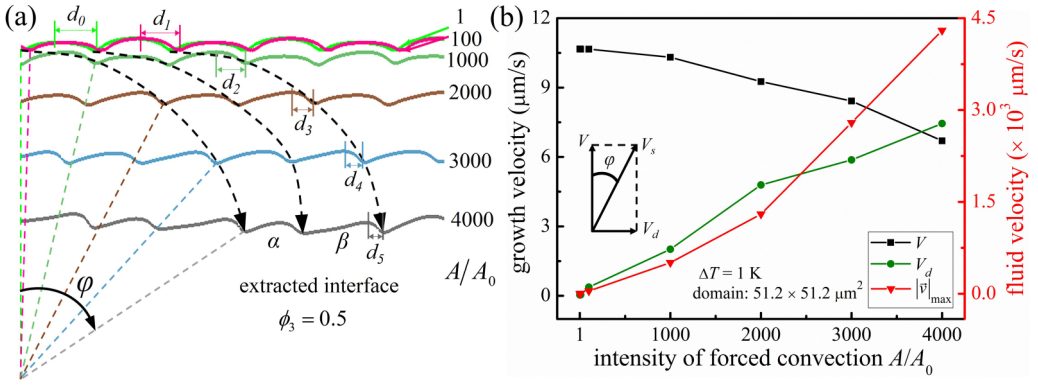

FIG. 8. (a) Illustration for the effect of the forced convection on interface morphology. (b) Growth velocity including V and V_d and the maximum fluid velocity vs the convection intensity.

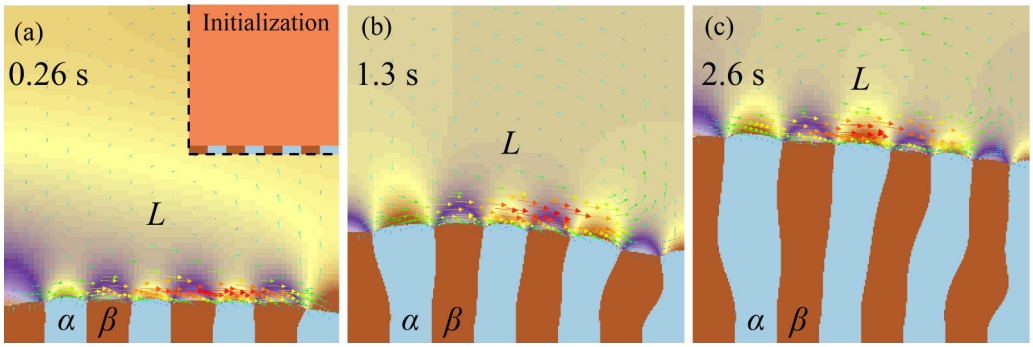

FIG. 9. Evolution of the eutectic lamellae under forced convection. The boundary conditions are zero-Neumann boundary condition for the solute and phase fields, and no-slip boundary condition for the flow field, respectively.

thus the lamellar tilting direction was not necessarily along the x^+, especially for the lamellae near the left side boundary.

Influenced by the forced flow, the rejected elements could be convected away in a timely manner, which enlarged the constitutional undercooling ΔT_c. To maintain a local thermodynamic equilibrium, the curvature undercooling, i.e., ΔT_r, must be decreased according to Eq. (18).Taking the α-L interface for instance, according to Eq. (19), the interfacial curvature was dependent on the contact angle θ_α, lamellar tilting angle φ, and interfacial half-width $S_{\alpha L}$. At the triple point (see Fig. 2), maintaining a local mechanical equilibrium requires

$$\sigma_{\alpha L}\sin\theta_\alpha + \sigma_{\beta L}\sin\theta_\beta = \sigma_{\alpha\beta}, \tag{23a}$$

$$\sigma_{\beta L}\cos\theta_\beta = \sigma_{\alpha L}\cos\theta_\alpha, \tag{23b}$$

where σ_{ij} represents the isotropic surface tension between the i and j phases. Equation (23) indicated that the contact angle was fixed during simulation. Considering that $S_{\alpha L}$ kept constant for the eutectic alloys during simulation, the adjustment of the average curvature was largely dependent on φ from Eq. (19). In detail, the decrease of ΔT_r was realized by increasing φ, and a larger convection intensity corresponded to a larger lamellar tilting angle before the lamellae lost its regular pattern [i.e., not satisfying Eqs. (19) or (23)].

As the convection intensity increased, the interfacial lamellar width λ_L maintained constant, but the lamellar spacing $\lambda(\lambda = \lambda_L \cdot \cos\varphi)$ decreased [see the definition of λ and λ_L in Figs. 4(a_8) and 4(b_8)]. In [2,7,8], however, the eutectic lamellar spacing increased with flow intensity. It is noted that in those studies, neither the asymmetric lamellar pattern nor the curvature undercooling closely connected with the phase width was considered, and λ_L and λ were not strictly distinguished either. Based on the Al-Cu alloy experiments, the examined width using a line scan by Lee *et al.* [3] was actually the interfacial lamellar width λ_L rather than the lamellar spacing λ, and they found that the flow effect on the interfacial lamellar width was rather small for the alloys with eutectic concentration. In this respect, our PFLB simulations for the eutectic growth agreed quite well with those observed in experiments [3].

V. COMPARISONS

In Sec. III, the JH theory was modified based on a weak convection assumption. To check the rationality of the modified JH theory, further PFLB simulations were performed to compare with the theoretical predictions by changing the undercooling and the initial lamellar spacing. To illustrate the difference between simulation results and theoretical predictions, the determined tilting angle and the interfacial lamellar spacing via the PFLB simulation were used as inputs for the modified JH theory to calculate the growth velocity [see Eq. (24)]. It is noted that the modified JH theory only

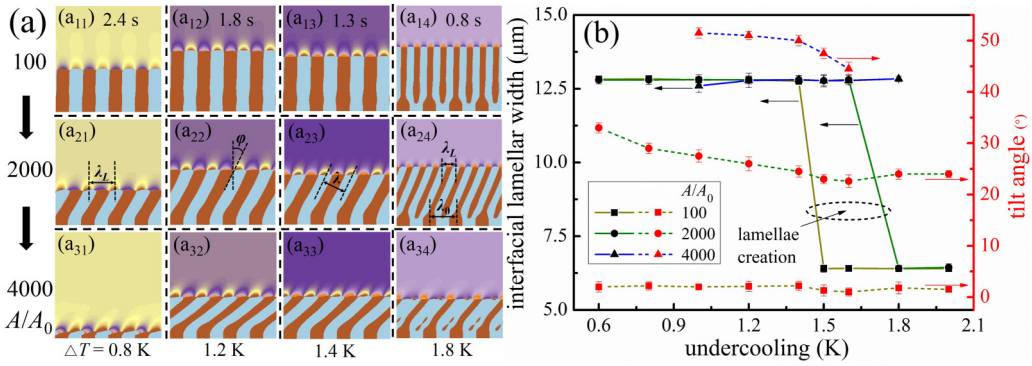

FIG. 10. Eutectic lamellar growth under different undercoolings. (a) Typical solute fields under four different undercoolings (i.e., 0.8, 1.2, 1.4, and 1.8 K, respectively). (b) Interfacial lamellar width and lamellar tilting angle vs the undercooling.

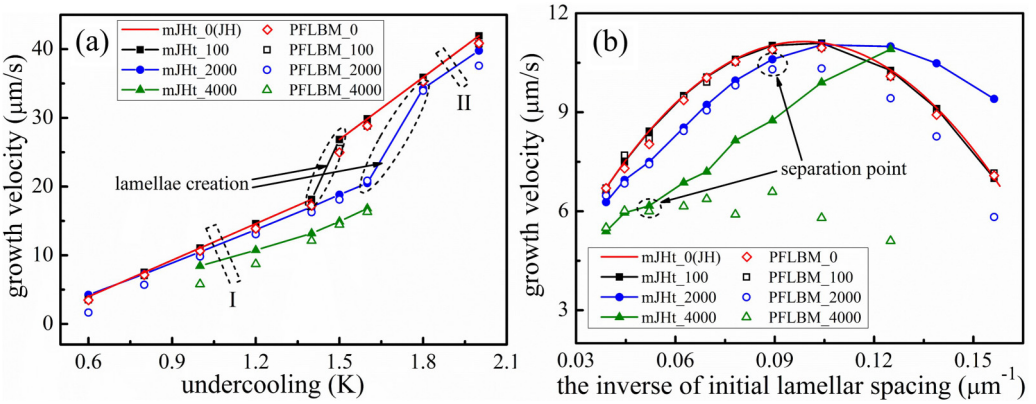

FIG. 11. Comparisons between the simulation results using the phase-field lattice-Boltzmann model (PFLBM) and those predicted by the modified JH theory (mJHt) under (a) different undercoolings and (b) different initial lamellar spacings. The numbers in the legend denote the magnification of the convection intensity.

considered a single-direction flow, i.e., the influence of the convection on the growth pattern was simplified.

The initial lamellar spacing was set to be 12.8 μm, and the undercooling was changed from 0.6 to 2.0 K. Figure 10(a) shows the solute fields according to four typical undercoolings (i.e., 0.8, 1.2, 1.4, and 1.8 K), and Fig. 10(b) shows the interfacial lamellar width and lamellar tilting angle versus the undercooling. As shown in Fig. 10(a), the stronger the flow, the larger the lamellar tilting angle. When the undercooling increased, the lamellar tilting angle tended to decrease, because increasing undercooling led to a larger driving force for the eutectic to grow, which compromised the effect of the forced flow. It is noted that if the undercooling was too small, e.g., 0.8 K for the force $A/A_0 = 4000$ [see Fig. 10(a_{31})], the eutectic couples did not have enough driving force to capture the precipitated elements, and further growth was inhibited. Besides, as a result of the spacing being approximately halved, the lamellae creation occurred when the undercooling reached a critical value, e.g., 1.5 and 1.8 K for the force $A/A_0 =$ 100 and 2000 respectively [see Figs. 10(a_{14}) and 10(a_{24})]. Similar behavior has been observed in experiments in which the lamellae creation was induced by increasing the growth velocity [4]. For other cases, the interfacial lamellar width equaled the initial lamellar spacing, i.e., 12.8 μm.

Derived from the modified JH theory, the eutectic growth velocity can be described as

$$V = -\frac{a\cos^2\varphi}{Q}\frac{1}{\lambda_L^2} + \frac{\Delta T\cos\varphi}{mQ}\frac{1}{\lambda_L}, \tag{24}$$

which indicates that the eutectic growth velocity is largely dependent on the lamellar tilting angle φ, the undercooling ΔT, and the interfacial lamellar width λ_L. Figure 11(a) shows the difference of the growth velocity between the PFLB simulation results and the ones predicted by the modified JH theory under different undercoolings. When the magnification of the convection intensity was 0 (i.e., nonconvection condition) or 100 times, the two velocity-undercooling curves almost overlapped. When the intensity was magnified 2000 times, the difference was still small, indicating that the modified JH theory agreed well with the simulations. But when the magnification reached 4000, the difference became remarkable, especially for the lower undercooling.

As shown in Fig. 11(a), when the interfacial lamellar width remained unchanged, the growth velocity increased linearly with the undercooling. The symbols I and II denoted the two linear segments separated by a transition stage where the interfacial lamellar width was halved during lamellae creation. As the flow intensity increased, the largest variation range of the lamellar tilting angle was less than 11°. The corresponding cos φ could be approximately unchanged because the maximum of $[\cos(\varphi + 11^\circ) - \cos\varphi]$ was less than 0.1 for the interested φ in Fig. 10(b). According to Eq. (24), the growth velocity will increase linearly with the undercooling if cos φ is constant. Therefore, in terms of variation trend, the simulations agreed well with the modified JH theory. Besides, both the slope [i.e., $\cos\varphi/(mQ\lambda_L)$] and intercept [i.e., $-a\cos^2\varphi/(Q\lambda_L^2)$] decreased with flow intensity except

TABLE I. Parameters of the linear fitting functions for simulated growth velocity vs the undercooling.

Source	Fitting function	Symbol	a	b	Pearson's r[a]	Adj. R square[b]
Fig. 11(b): PFLBM_0	$y = a \times x + b$	I	17.116	−6.6485	0.999 71	0.999 22
		II	31.573	−21.977	0.998 12	0.994 37
Fig. 11(b): PFLBM_100		I	17.028	−7.0285	0.999 60	0.998 94
		II	30.592	−20.62	0.998 97	0.996 91
Fig. 11(b): PFLBM_2000		I	14.823	−4.894	0.969 97	0.979 34
		II	20.747	−1.6231	0.984 46	0.938 32
Fig. 11(b): PFLBM_4000		I	18.585	−13.321	0.997 36	0.992 97

[a]Pearson's r: reflect the linear correlation between two variables, and the closer to one the absolute value, the stronger the correlation [58].
[b]Adj. R square: an adjusted version of R square, which satisfies that the closer to one, the more accurate the fitting function [58].

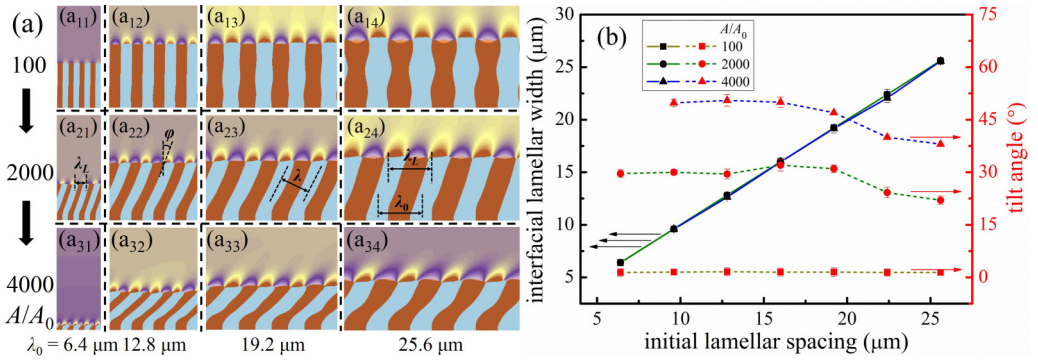

FIG. 12. Eutectic lamellar growth under different initial lamellar spacings. (a) Typical solute fields under four different initial lamellar spacings (i.e., 6.4, 12.8, 19.2, and 25.6 μm, respectively). (b) Interfacial lamellar width and lamellar tilting angle vs the initial lamellar spacing.

at $A/A_0 = 4000$. This is because both terms were monotonic decreasing functions of lamellar tilting angle, and the larger the flow intensity, the larger the tilting angle. But when the flow intensity was too large, e.g., $A/A_0 = 4000$, the weak convection assumption was no longer satisfied. Accordingly, the eutectic growth could not be described by the modified JH theory. Related linear fitting parameters are provided in Table I.

Figures 12(a) shows the simulated solute fields according to 12 different cases. The undercoolings were all 1.0 K, and the chosen initial lamellar spacings were 6.4, 12.8, 19.2, and 25.6 μm, respectively. Both the initial lamellar spacing and flow intensity had significant effects on the eutectic growth including the lamellar tilting angle and morphological shape. As the initial lamellar spacing increased, the eutectic pattern changed from being parallel to oscillating, as show in Figs. 12(a_{11})–12(a_{14}). The pattern transition was also observed by changing the flow intensity. Taking $\lambda_0 = 25.6\,\mu$m for instance, the lamellar pattern changed from the oscillating to parallel pattern when the flow intensity was increased from 100 to 2000 times [see Figs. 12(a_{14}) and 12(a_{24})].

The eutectic growth was controlled by the interaction between solute transport and curvature effect. As the lamellar spacing increased, the curvature effect became more significant, leading to an oscillating growth pattern [59–61]. But as the flow intensity increased, the solute transport capacity was strengthened, and accordingly the eutectic lamellae tended to grow in a parallel mode again. It is noted that if the lamellar spacing was too small, the precipitated elements would be entirely flushed away by the flow, which reduced the number of the elements supplying the eutectic growth, and thus inhibited further growth of the eutectic.

Figure 12(b) shows the interfacial lamellar width and lamellar tilting angle versus the initial lamellar spacing λ_0. The interfacial lamellar width λ_L was almost the same as the initial lamellar spacing λ_0, while the lamellar tilting angle exhibited a significant decrease when λ_0 was relatively large, e.g., from 31° at $\lambda_0 = 19.2\,\mu$m to 24.2° at $\lambda_0 = 22.4\,\mu$m for $A/A_0 = 2000$. As the initial lamellar spacing became larger, the interface length of one eutectic couple increased and thus more interfacial solute exchange happened, which compromised the effect of forced convection and led to a decrease of the lamellar tilting angle.

Figure 11(b) shows the comparison of the PFLB simulation results with those predicted by the modified JH theory under different lamellar spacings. Similar to Fig. 11(a), when the flow intensity was small (e.g., $A/A_0 \leqslant 100$), the PFLB simulation results agreed with those predicted by the modified JH theory. However, a larger difference exhibited as the flow intensity became larger. A separation point was introduced to illustrate that the relative deviation between the two results (theoretical predictions minus PFLB simulated ones divided by theoretical predictions) approached 5%. Taking $A/A_0 = 2000$ for instance, if the initial lamellar spacing was smaller than 11.2 μm [i.e., $1/\lambda_0 \geqslant 0.089\,29\,\mu\text{m}^{-1}$; see the right of the separation point in Fig. 11(b)], the simulation results deviated significantly from those predicted by the modified JH theory, and the smaller the spacing, the larger the deviation. Because when the flow intensity was constant, decreasing the lamellar spacing would lead to an increasing effect of the convection on the solute movement in front of the S-L interface. If the

TABLE II. Parameters of the quadratic fitting functions for simulated growth velocity vs the inverse of the lamellar spacing.

Source	Fitting function	a	b	c	Reduced chi square[a]	Adj. R square[b]
Fig. 13(b): PFLBM_0	$y = a \times x^2 + b \times x + c$	−1258.7	250.46	−1.352 25	0.043 98	0.983 60
Fig. 13(b): PFLBM_100		−1243.1	245.12	−0.925 58	0.010 63	0.994 46
Fig. 13(b): PFLBM_2000		−1174.8	225.49	−0.8820	0.039 72	0.9822

[a]Reduced chi square: equivalent to residual mean square in the analysis of variance and the smaller the value, i.e., closer to zero, the higher the fitting degree [58].

[b]Adj. R square: an adjusted version of R square, which satisfies that the closer to one, the more accurate the fitting function [58].

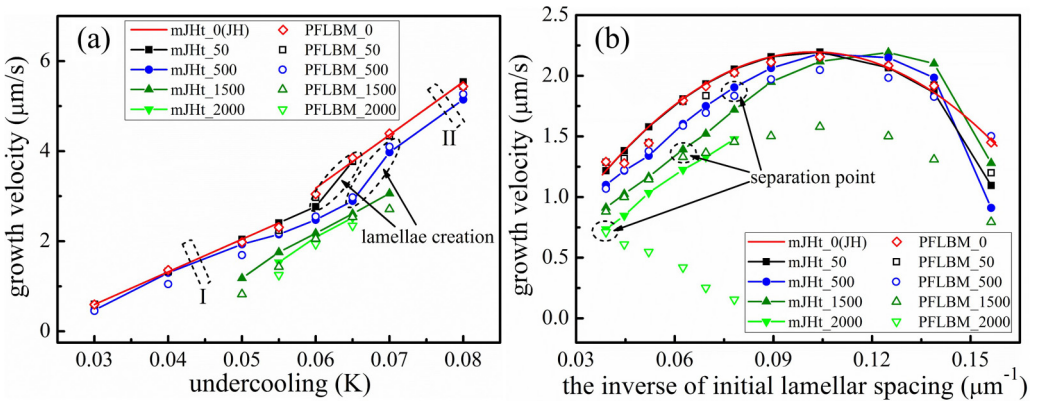

FIG. 13. Comparisons between the simulation results using the phase-field lattice-Boltzmann model (PFLBM) and those predicted by the modified JH theory (mJHt) under (a) different undercoolings and (b) different initial lamellar spacings for the CBr_4-C_2Cl_6 alloy. The numbers in the legend denote the magnification of the convection intensity.

flow intensity was increased 4000 times, the initial lamellar spacing at the separation point became 19.2 μm, indicating that λ_0 at the separation point would increase with the flow intensity. The variation of the longitudinal growth velocity versus the inverse of the lamellar spacing could be best described by a quadratic fitting function for $A/A_0 \leqslant 2000$, which was consistent with Eq. (24) if the slight change of cos φ was reasonably ignored. Detailed parameters are provided in Table II.

To further investigate the influence of the forced convection, simulations were performed on another commonly used transparent alloy, i.e., the CBr_4-C_2Cl_6 alloy. The largest difference between this alloy and the Al-Cu alloy was the interfacial width ratio of coexisting solid phases (i.e., $\zeta = S_{\beta L}/S_{\alpha L}$). This value is approximately 1:2 for the CBr_4-C_2Cl_6 alloy and 1:1 for the Al-Cu alloy. Figure 13 shows the comparison of the PFLB simulation results with those predicted by the modified JH theory. As the undercooling increased, the growth velocity increased linearly and the curves overlapped for weaker flow intensity scenarios, e.g., $A/A_0 \leqslant 500$. When the flow intensity was relatively large, e.g., $A/A_0 \geqslant 1500$, the difference between the simulation results and those predicted using the modified JH theory would increase with decreasing undercooling, as shown in Fig. 13(a). When the initial lamellar spacing was changed, a larger flow intensity led to a larger difference between the simulation and theory. The modified JH theory agreed well with the simulation results only at the larger spacing for stronger convection, i.e., at the left of the separation points in Fig. 13(b).

VI. CONCLUSIONS

A modified Jackson-Hunt theory was proposed to investigate the eutectic growth under a single-direction flow. The presence of the convection altered the solute distribution and tilted the eutectic lamellae. The eutectic growth under forced convection was reproduced by incorporating an external force inside the phase-field lattice-Boltzmann model. Comparisons between the PFLB simulation results and the theoretical predictions were performed, and the following conclusions can be drawn:

(1) A modified JH theory, i.e., $\frac{\Delta T}{m} = \frac{V\lambda_L Q}{\cos\varphi} + \frac{a\cos\varphi}{\lambda_L}$, is developed to predict the tilting lamellar eutectic growth, where φ is the lamellar tilting angle measuring the flow intensity. ΔT is the undercooling, V is the longitudinal growth velocity, λ_L is the interfacial lamellar width, and m, Q, and a are constants identical to those in the classical JH theory. The modified JH theory can be restored to the classical JH theory by taking $\varphi = 0$.

(2) The forced convection changes the solute distribution at the solid-liquid interface and shifts the concentration isolines along the flow direction. The change of the solute transport capacity induced by the flow leads to asymmetrical growth patterns about the centerlines of the solid phases. To maintain local thermodynamic equilibrium, a tilting pattern is exhibited by adjusting the interfacial curvature, and a stronger flow intensity causes a larger tilting angle.

(3) Under weak convection, the phase-field lattice-Boltzmann simulation results agree well with those predicted by the modified JH theory. The modified JH theory becomes unsuitable if the undercooling or the initial lamellar spacing is too small. In the latter case, the flow effect becomes too significant to match the weak convection assumption during the derivation of the modified JH theory.

(4) According to the PFLB simulation results, the growth velocity increases linearly with the undercooling while it changes quadratically with the inverse of the initial lamellar spacing. A much stronger flow inhibits further lamellar eutectic growth due to the lack of elements which are convected away by the flow in a timely manner.

ACKNOWLEDGMENTS

This work was financially supported by the National Natural Science Foundation of China (Grants No. U1537202 and No. 51701104), the Tsinghua-General Motors International Collaboration Project (Grant No. 20153000354), the Tsinghua University Initiative Scientific Research Program (Grant No. 20151080370), and the Tsinghua Qingfeng Scholarship (THQF2018-15). The authors would also like to thank the National Laboratory for Information Science and Technology in Tsinghua University for access to supercomputing facilities.

APPENDIX A: DETERMINATION OF THE EXPRESSIONS B_0' AND B_n' IN EQ. (7b)

To determine B_0' and B_n' in Eq. (7b), the first derivative of the solute concentration $C(X, Y)$ with respect to Y is deduced as follows:

$$\left.\frac{\partial C(X,Y)}{\partial Y}\right|_{Y=0} = -\Lambda(1+\Theta)B'_0 + (1+\Theta)\sum_{n=1}^{\infty} B'_n\left[(-2n\pi)\left(\cos(2n\pi X) - \frac{2}{\Lambda^2}\frac{\Theta}{1+\Theta}\sin(2n\pi X)\right) + \frac{\Theta}{(1+\Theta)\Lambda}\sin(2n\pi X)\right]. \tag{A1}$$

Integrating from 0 to 1 for X, we can obtain

$$\int_0^1 \left.\frac{\partial C(X,Y)}{\partial Y}\right|_{Y=0} dX = -\Lambda(1+\Theta)B'_0. \tag{A2}$$

Based on the flux conditions near the S-L interface ($Y = 0$), i.e., Eqs. (13c) and (13d), the following one is deduced:

$$\int_0^1 \left.\frac{\partial C(X,Y)}{\partial Y}\right|_{Y=0} dX = \int_0^{S_{\alpha L}/\lambda_L} \frac{-\Lambda C_L^{\alpha}(1-k_\alpha)}{\cos\varphi} dX + \int_{S_{\alpha L}/\lambda_L}^{1-(S_{\alpha L}/\lambda_L)} \frac{-\Lambda C_L^{\beta}(1-k_\beta)}{\cos\varphi} dX + \int_{1-(S_{\alpha L}/\lambda_L)}^{1} \frac{-\Lambda C_L^{\alpha}(1-k_\alpha)}{\cos\varphi} dX = \frac{-\Lambda\left[S_{\alpha L}C_L^{\alpha}(1-k_\alpha) + S_{\beta L}C_L^{\beta}(1-k_\beta)\right]}{(S_{\alpha L}+S_{\beta L})\cos\varphi}. \tag{A3}$$

Thus from Eqs. (A2) and (A3), B_0' is deduced as follows:

$$B'_0 = \frac{S_{\alpha L}C_L^{\alpha}(1-k_\alpha) + S_{\beta L}C_L^{\beta}(1-k_\beta)}{(1+\Theta)(S_{\alpha L}+S_{\beta L})\cos\varphi}. \tag{A4}$$

Similarly, after multiplying Eqs. (13c), (13d), and (A1) by $\cos(2k\pi x)$ (k is a positive integer staring from 1), respectively, we can deduce the expression of B_n'. For Eqs. (13c) and (13d), we can obtain

$$\int_0^1 \left(\left.\frac{\partial C(X,Y)}{\partial Y}\right|_{Y=0}\right)\cos(2k\pi X)dX = \frac{\Lambda\left[C_L^{\beta}(1-k_\beta) - C_L^{\alpha}(1-k_\alpha)\right]}{k\pi\cos\varphi}\sin\left(\frac{k\pi S_{\alpha L}}{S_{\alpha L}+S_{\beta L}}\right). \tag{A5}$$

For Eq. (A1), after multiplication and integration from 0 to 1, we can obtain

$$\begin{aligned}&\int_0^1 \left(\left.\frac{\partial C(X,Y)}{\partial Y}\right|_{Y=0}\right)\cos(2k\pi X)dX = (1+\Theta)\\ &\times\int_0^1 \sum_{n=1}^{\infty} B'_n\left[(-2n\pi)\left(\cos(2n\pi X) - \frac{2}{\Lambda^2}\frac{\Theta}{1+\Theta}\sin(2n\pi X)\right) + \frac{\Theta}{(1+\Theta)\Lambda}\sin(2n\pi X)\right]\cos(2k\pi X)dX\\ &= -k\pi B'_k(1+\Theta)\end{aligned} \tag{A6}$$

in which the simplification process takes advantage of the orthogonality of trigonometric functions, i.e.,

$$\int_0^1 \cos(2n\pi X)\cos(2k\pi X)dX = \frac{1}{2}\delta_{nk}, \tag{A7a}$$

$$\int_0^1 \sin(2n\pi X)\cos(2k\pi X)dX = 0, \tag{A7b}$$

where δ_{nk} is a Kronecker delta, i.e., δ_{nk} is 1 when n equals k and 0 otherwise.

Thus from Eqs. (A5) and (A6), B_n' can be deduced as follows:

$$B'_n = \frac{\Lambda\left[C_L^{\alpha}(1-k_\alpha) - C_L^{\beta}(1-k_\beta)\right]}{(1+\Theta)(n\pi)^2\cos\varphi}\sin\left(\frac{n\pi S_{\alpha L}}{S_{\alpha L}+S_{\beta L}}\right). \tag{A8}$$

APPENDIX B: DERIVATION OF THE SPECIAL SOLUTION OF EQ. (9b)

Similar to Eq. (5b), Eq. (9b) is also a nonhomogeneous equation, whose solution is presented as

$$C_1(X,Y) = C_1^*(X,Y) + C_0(X,Y), \tag{B1}$$

where $C_1^*(X, Y)$ is the special solution and $C_0(X, Y)$ is the general solution of the associated homogeneous equation, i.e., Eq. (7b). Inserting Eqs. (7b) and (B1) into Eq. (9b), the following form is obtained:

$$\frac{\partial^2 C_1^*(X,Y)}{\partial X^2} + \frac{\partial^2 C_1^*(X,Y)}{\partial Y^2} + \Lambda \frac{\partial C_1^*(X,Y)}{\partial Y} = \sum_{n=1}^{\infty} B'_n(-2n\pi Y)\sin(2n\pi X)\exp(-2n\pi Y). \tag{B2}$$

Based on the superposition principle, Eq. (B2) is simplified as

$$\frac{\partial^2 C_{1n}^*(X,Y)}{\partial X^2} + \frac{\partial^2 C_{1n}^*(X,Y)}{\partial Y^2} + \Lambda \frac{\partial C_{1n}^*(X,Y)}{\partial Y} = -B'_n(2n\pi Y)\sin(2n\pi X)\exp(-2n\pi Y), \tag{B3}$$

where n is a positive integer staring from 1, and $C_{1n}^*(X, Y)$ is the eigensolution of $C_1^*(X, Y)$. By integrating Eq. (B3) and considering $\Lambda \ll 4n\pi$, we can obtain

$$C_{1n}^*(X,Y) = \frac{1}{\Lambda}\left(Y + \frac{1}{2n\pi} - \frac{2}{\Lambda}\right)B'_n \sin(2n\pi X)\exp(-2n\pi Y) \approx \left(\frac{Y}{\Lambda} - \frac{2}{\Lambda^2}\right)B'_n \sin(2n\pi X)\exp(-2n\pi Y). \tag{B4}$$

Thus, by summing the eigensolutions Eq. (B4) for $n = 1, 2, \ldots$, the special solution is deduced as follows:

$$C_1^*(X,Y) = \left(\frac{Y}{\Lambda} - \frac{2}{\Lambda^2}\right)\sum_{n=1}^{\infty} B'_n \sin(2n\pi X)\exp(-2n\pi Y). \tag{B5}$$

APPENDIX C: COMPUTATION OF THE AVERAGE CURVATURE

Taking the α-L interface for instance, as shown in Fig. 14, the contact angles $\theta_{\alpha L}$ and $\theta_{\alpha R}$ are equal due to the mechanism equilibrium at the triple points A and B, i.e., Eqs. (23a) and (23b). Then the average curvature can be deduced as follows:

$$\begin{aligned}
\langle\kappa_\alpha(x)\rangle &= \frac{1}{2S_{\alpha L}}\int_{-S_{\alpha L}}^{S_{\alpha L}} \kappa_\alpha(x)dx \\
&= \frac{1}{2S_{\alpha L}}\int_{-S_{\alpha L}}^{S_{\alpha L}} \frac{|d^2I/dx^2|}{[1+(dI/dx)^2]^{3/2}}dx \\
&= -\frac{1}{2S_{\alpha L}}\{\sin[\pi - (\theta_{\alpha R}+\varphi)] - \sin(\theta_{\alpha L}-\varphi)\} \\
&= \frac{1}{S_{\alpha L}}\left(\sin\frac{\theta_{\alpha R}+\theta_{\alpha L}}{2}\cos\frac{\theta_{\alpha R}-\theta_{\alpha L}+2\varphi}{2}\right) \\
&= \frac{\sin\theta_\alpha\cos\varphi}{S_{\alpha L}},
\end{aligned} \tag{C1}$$

where $\theta_\alpha = \theta_{\alpha R} = \theta_{\alpha L}$ denotes the contact angle at the α-L interface.

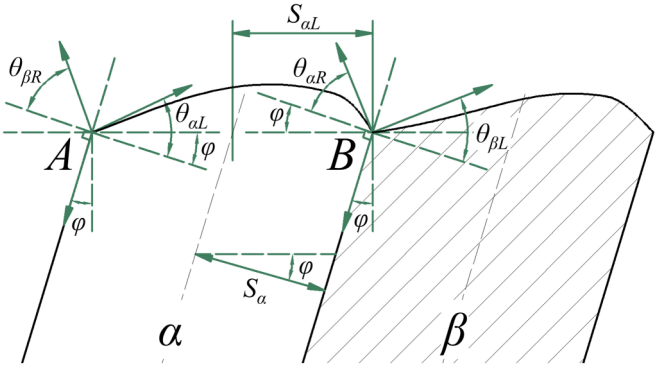

FIG. 14. Schematic diagram of contact angles at the triple point of tilted eutectic lamellae.

APPENDIX D: SOLUTE REDISTRIBUTION NEAR THE INTERFACE

In the present phase-field lattice-Boltzmann model, the overall mass balance is satisfied because no source terms are present. But this does not necessarily mean that the equilibrium concentration in the liquid should equal the initial eutectic concentration. On the other hand, the equilibrium concentration in the liquid is dependent on the average concentration in the solid phases.

For the Al-Cu eutectic alloy, the average concentration in the solid phases is not equal to the concentration at the eutectic point. During eutectic solidification, the deviation from the eutectic concentration in the solid phases needs to be compensated by adjusting the equilibrium concentration in front of the S-L interface. In other words, if the liquid concentration keeps at the initial concentration, the mass conservation will not be maintained unless the average concentration in the solid phase equals the eutectic concentration.

Accordingly, we assume an ideal alloy with a symmetrical phase diagram according to the thermophysical parameters of the α phase in the Al-Cu eutectic alloy. Table III lists the parameters used during simulation, and the following two points are highlighted:

(1) Letting $k_\beta = 2 - k_\alpha$ for the ideal alloy is to ensure that the eutectic point is located at the middle point of the eutectic line, i.e., $C_\alpha + C_\beta = 2C_E$, where $C_\alpha = k_\alpha C_E$ and $C_\beta = k_b C_E$ are the solute concentration of the α and β phases at the eutectic temperature, respectively.

(2) Letting $m_\beta = -m_\alpha$, and $C_E = 0.5$ mol frac for the ideal alloy is to ensure that the phase diagram is symmetrical about the eutectic point.

Figure 15 shows the distribution of the solute concentration at the initial time and steady state for the ideal alloy and Al-Cu alloys without convection. The equilibrium solute concentration in both solid and liquid phases keeps the same as the initial concentration for the ideal alloy [see Figs. 15(a) and 15(b)], i.e., 0.5 mol frac, indicating the eutectic solidification

TABLE III. Thermophysical parameters of the Al-Cu and ideal alloys [35,37,62,63].

Parameters	Al-Cu		Ideal
D_L (solute diffusivity in liquid, m^2/s)		3×10^{-9}	
D_S (solute diffusivity in solid, m^2/s)		3×10^{-13}	
m_α (liquidus slope of α phase at eutectic temperature, K/mol frac)		-1050	
m_β (liquidus slope of β phase at eutectic temperature, K/mol frac)	488		1050
k_α (partition coefficient in α phase to the liquid phase)		0.1445	
k_β (partition coefficient in β phase to the liquid phase)	1.85		1.8555
T_E (eutectic temperature, K)		821.4	
C_E (eutectic concentration, mol frac)	0.173		0.5
$\sigma_{\alpha L}$ (α-L interface energy, J/m^2)		160.01×10^{-3}	
$\sigma_{\beta L}$ (β-L interface energy, J/m^2)	88.363×10^{-3}		160.01×10^{-3}
$\sigma_{\alpha\beta}$ (α-β interface energy, J/m^2)		219.484×10^{-3}	

is globally equivalent to the growth of a single phase. But for the Al-Cu eutectic alloy, $k_\beta + k_\alpha < 2$ and $m_\beta \neq -m_\alpha$, the average concentration in the solid phases is smaller than the eutectic concentration, and it keeps increasing as the solidification proceeds. To maintain the mass conservation, the increase of the solute concentration in the solid phases needs to be balanced by decreasing the solute concentration in the liquid, resulting in that the liquid equilibrium concentration is smaller than the initial solute concentration [see Figs. 15(c) and 15(d)].

Furthermore, if the domain height is high enough, only the concentration near the interface will be adjusted, while the far-field solute concentration can keep at the initial value. As shown in Fig. 16, the domain height is eight times larger than the domain width, and after undergoing a transition region near the interface, the liquid concentration reaches the initial value.

It is noted that whether the equilibrium solute concentration equals the initial value exhibits little influence on the eutectic growth. Under the certain equilibrium concentration, the solute concentration in front of the S-L interface exhibits the opposite variation rule between the α and β phases, which maintains the cooperative growth of two coexisting solid phases and forms a stable solute transition layer. It is accepted that the presence of convection affects the lamellar growth pattern by changing the interfacial solute distribution. In this work, we focus on the change due to convection by comparing the results with and without flow, and obtain a

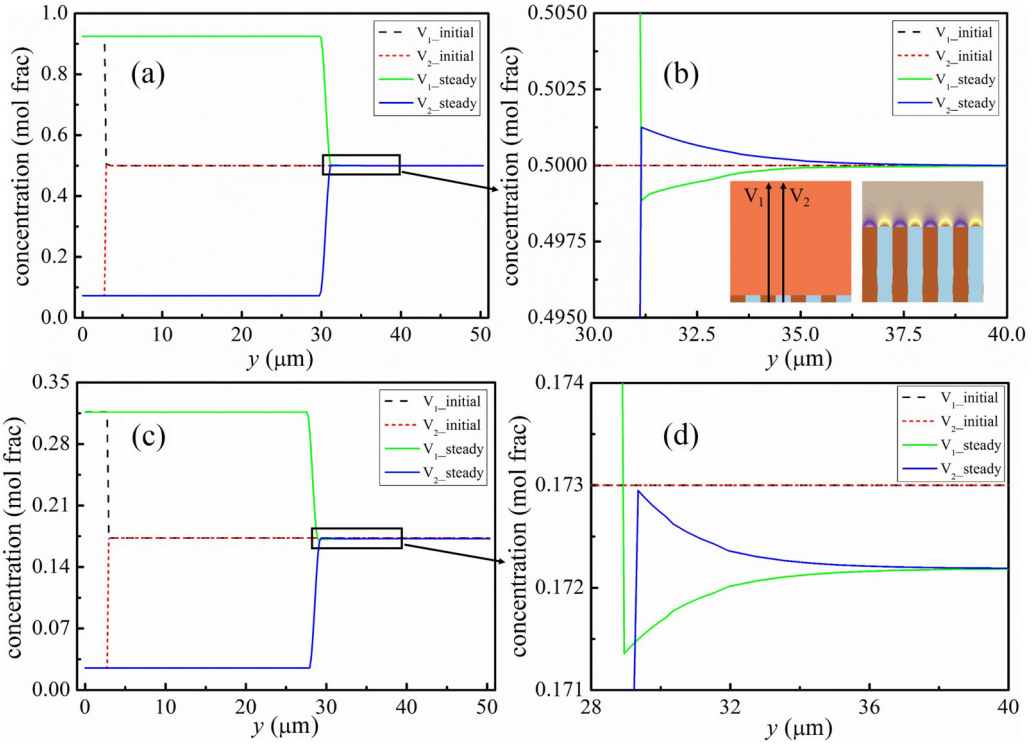

FIG. 15. Distribution of the solute concentration along the y axis (see V_1 and V_2) at the initial time and the steady state for the ideal alloy (the first row) and Al-Cu alloy (the second row). Panels (b) and (d) are the local enlarged images of the solute concentration near the interface for the ideal alloy and Al-Cu alloy, respectively.

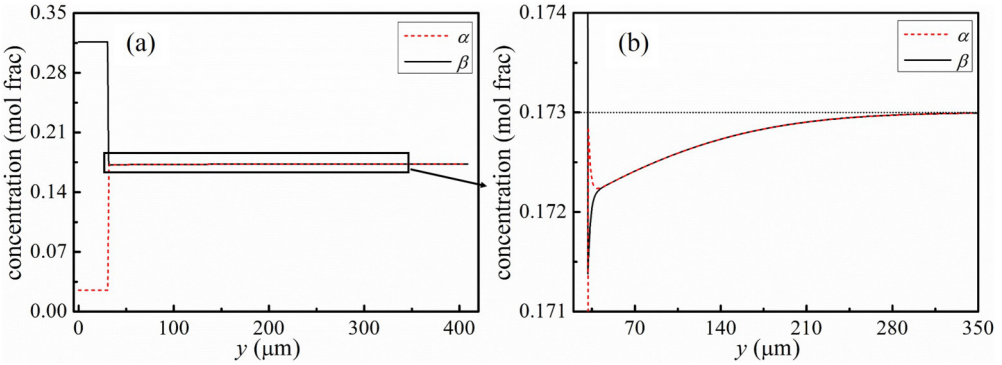

FIG. 16. Liquid solute concentration vs the distance along the direction perpendicular to the solid-liquid interface for the Al-Cu alloy. (b) Local enlarged image of the solute concentration near the interface. The domain height is eight times larger than the domain width.

quantitative relation among the growth velocity, undercooling, and lamellar spacing, which is independent of the specific concentration value or the alloy systems (e.g., the Al-Cu, CBr_4-C_2Cl_6, and the ideal alloys).

[1] K. A. Jackson and J. D. Hunt, Trans. Metall. Soc. AIME **236**, 1129 (1966).
[2] V. Baskaran and W. R. Wilcox, J. Cryst. Growth **67**, 343 (1984).
[3] J. H. Lee, S. Liu, and R. Trivedi, Metall. Mater. Trans. A **36**, 3111 (2005).
[4] J. A. Dantzig and M. Rappaz, *Solidification* (EPFL, Lausanne, 2009).
[5] S. Xiong, J. Du, Z. Guo, M. Yang, M. Wu, C. Bi, and Y. Cao, Acta Metall Sin **54**, 174 (2018).
[6] S. Akamatsu, K. Lee, and W. Losert, J. Cryst. Growth **289**, 331 (2006).
[7] J. M. Quenisset and R. Naslain, J. Cryst. Growth **54**, 465 (1981).
[8] D. Ma, W. Q. Jie, Y. Li, and S. C. Ng, Acta Mater. **46**, 3203 (1998).
[9] W. M. Wang, Z. G. Liu, J. M. Liu, and X. Y. Chen, J. Cryst. Growth **240**, 313 (2002).
[10] R. Siquieri and H. Emmerich, Philos. Mag. **91**, 45 (2011).
[11] Y. J. Chen and S. H. Davis, Acta Mater. **50**, 2269 (2002).
[12] F. Drolet, K. R. Elder, M. Grant, and J. M. Kosterlitz, Phys. Rev. E **61**, 6705 (2000).
[13] S. Gyoon Kim, W. Tae Kim, T. Suzuki, and M. Ode, J. Cryst. Growth **261**, 135 (2004).
[14] L. Rátkai, A. Szállás, T. Pusztai, T. Mohri, and L. Gránásy, J. Chem. Phys. **142**, 154501 (2015).
[15] A. Zhang, Z. Guo, and S. M. Xiong, J. Appl. Phys. **121**, 125101 (2017).
[16] A. Zhang, Z. Guo, and S. Xiong, China Foundry **14**, 373 (2017).
[17] N. Moelans, B. Blanpain, and P. Wollants, Calphad **32**, 268 (2008).
[18] W. J. Boettinger, J. A. Warren, C. Beckermann, and A. Karma, Annu. Rev. Mater. Res. **32**, 163 (2002).
[19] J. Du, A. Zhang, Z. Guo, M. Yang, M. Li, F. Liu, and S. Xiong, Acta Mater. **161**, 35 (2018).
[20] I. Steinbach, Modelling Simul. Mater. Sci. Eng. **17**, 073001 (2009).
[21] D. Sun, M. Zhu, S. Pan, and D. Raabe, Acta Mater. **57**, 1755 (2009).
[22] X. Zhang, J. Kang, Z. Guo, S. Xiong, and Q. Han, Comput. Phys. Commun. **223**, 18 (2018).
[23] C. Beckermann, H. J. Diepers, I. Steinbach, A. Karma, and X. Tong, J. Comput. Phys. **154**, 468 (1999).
[24] X. Tong, C. Beckermann, A. Karma, and Q. Li, Phys. Rev. E **63**, 061601 (2001).
[25] C. W. Lan and C. J. Shih, J. Cryst. Growth **264**, 472 (2004).
[26] Z. Guo, J. Mi, S. Xiong, and P. S. Grant, J. Comput. Phys. **257**, 278 (2014).
[27] S. Succi, R. Benzi, and F. Higuera, Physica D **47**, 219 (1991).
[28] A. Fakhari, M. Geier, and T. Lee, J. Comput. Phys. **315**, 434 (2016).
[29] T. Krüger, H. Kusumaatmaja, A. Kuzmin, O. Shardt, G. Silva, and E. M. Viggen, *The Lattice Boltzmann Method Principles and Practice* (Springer, Switzerland, Cham, 2017).
[30] F. J. Higuera and S. Succi, Europhys. Lett. **8**, 517 (1989).
[31] F. J. Higuera, S. Succi, and R. Benzi, Europhys. Lett. **9**, 345 (1989).
[32] R. Benzi, S. Succi, and M. Vergassola, Phys. Rep. **222**, 145 (1992).
[33] W. Miller, S. Succi, and D. Mansutti, Phys. Rev. Lett. **86**, 3578 (2001).
[34] D. Medvedev, T. Fischaleck, and K. Kassner, Phys. Rev. E **74**, 031606 (2006).
[35] S. Sakane, T. Takaki, M. Ohno, Y. Shibuta, T. Shimokawabe, and T. Aoki, J. Cryst. Growth **483**, 147 (2018).
[36] A. Zhang, J. Du, Z. Guo, Q. Wang, and S. Xiong, Metall. Mater. Trans. B (2018), doi: 10.1007/s11663-018-1418-1
[37] A. Zhang, Z. Guo, and S. M. Xiong, Phys. Rev. E **97**, 053302 (2018).
[38] Z. Guo and S. M. Xiong, Comput. Phys. Commun. **190**, 89 (2015).
[39] M. Serefoglu, R. E. Napolitano, and M. Plapp, Phys. Rev. E **84**, 011614 (2011).
[40] M. Perrut, A. Parisi, S. Akamatsu, S. Bottin-Rousseau, G. Faivre, and M. Plapp, Acta Mater. **58**, 1761 (2010).

[41] A. Parisi and M. Plapp, Europhys. Lett. **90**, 26010 (2010).
[42] A. Parisi and M. Plapp, Acta Mater. **56**, 1348 (2008).
[43] J. Hötzer, P. Steinmetz, M. Jainta, S. Schulz, M. Kellner, B. Nestler, A. Genau, A. Dennstedt, M. Bauer, H. Köstler, and U. Rüde, Acta Mater. **106**, 249 (2016).
[44] J. Hötzer, P. Steinmetz, A. Dennstedt, A. Genau, M. Kellner, I. Sargin, and B. Nestler, Acta Mater. **136**, 335 (2017).
[45] I. Steinbach and F. Pezzolla, Physica D **134**, 385 (1999).
[46] Y. H. Qian, D. D'Humières, and P. Lallemand, Europhys. Lett. **17**, 479 (1992).
[47] Z. Guo, C. Zheng, and B. Shi, Phys. Rev. E **65**, 046308 (2002).
[48] J. Du, A. Zhang, Z. Guo, M. Yang, M. Li, and S. Xiong, ACS Omega **2**, 8803 (2017).
[49] J. Du, Z. Guo, A. Zhang, M. Yang, M. Li, and S. Xiong, Sci. Rep.UK **7**, 13600 (2017).
[50] J. Du, A. Zhang, Z. Guo, M. Yang, M. Li, and S. Xiong, Intermetallics **95**, 119 (2018).
[51] J. Du, A. Zhang, Z. Guo, M. Yang, M. Li, and S. Xiong, Phys. Rev. Mater. **2**, 83402 (2018).
[52] M. Berger and I. Rigoutsos, IEEE Trans. Syst. Man Cybern. **21**, 1278 (1991).
[53] S. R. Coriell, G. B. McFadden, W. F. Mitchell, B. T. Murray, J. B. Andrews, and Y. Arikawa, J. Cryst. Growth **224**, 145 (2001).
[54] R. Caram, S. Chandrasekhar, and W. R. Wilcox, J. Cryst. Growth **106**, 294 (1990).
[55] M. H. Holmes, *Introduction to Perturbation Methods* (Springer, New York, 2013).
[56] P. Magnin and R. Trivedi, Acta Metall. Mater. **39**, 453 (1991).
[57] R. S. Maier, R. S. Bernard, and D. W. Grunau, Phys Fluids **8**, 1788 (1996).
[58] R. A. Johnson and D. W. Wichern, *Applied Multivariate Statistical Analysis* (Pearson, Prentice-Hall, Upper Saddle River, NJ, 2007).
[59] A. Karma, Phys. Rev. Lett. **59**, 71 (1987).
[60] A. Karma and A. Sarkissian, Metall. Mater. Trans. A **27**, 635 (1996).
[61] M. F. Zhu and C. P. Hong, Phys. Rev. B **66**, 155428 (2002).
[62] N. Maraşli and J. D. Hunt., Acta Mater. **44**, 1085 (1996).
[63] M. Gündüz and J. D. Hunt, Acta Mater. **33**, 1651 (1985).